International Journal of Solids and Structures 118–119 (2017) 41–57

Contents lists available at ScienceDirect

International Journal of Solids and Structures

journal homepage: www.elsevier.com/locate/ijsolstr

On crack propagation in brittle material using the distinct lattice spring model

Chao Jiang[a,b], Gao-Feng Zhao[a,*], Nasser Khalili[b]

[a] State Key Laboratory of Hydraulic Engineering Simulation and Safety, School of Civil Engineering, Tianjin University, Beiyangyuan Campus, Jinnan District, 300350 Tianjin, China

[b] School of Civil and Environmental Engineering, The University of New South Wales, Sydney, 2052 NSW, Australia

ARTICLE INFO

Article history:
Received 13 June 2016
Revised 16 April 2017
Available online 26 April 2017

Keywords:
Crack propagation
Fracture mechanics
Lattice spring model
Brittle materials

ABSTRACT

With the rapid development of high-performance computing, Lattice Spring Models (LSMs) using a simple fracturing law demonstrate many prospects for simulating crack propagation in brittle solids. In this paper, a comprehensive study on crack propagation in brittle material is conducted using the distinct lattice spring model (DLSM) with high-performance computing and physical tests on crack propagation in brittle material from this work and the literature. The relationship between the simple fracturing law and the fracture criterion based on linear elastic fracture mechanics is investigated for the first time. The work involved includes the correlation between the Stress Intensity Factor (SIF) and spring deformation, the influence of the particle size on fracture toughness, and the relationship between the micro-spring failure and the critical stress intensity factors. Our results indicate that the simple fracturing law based on spring deformation may be easier and more fundamental for understanding crack propagation in brittle materials than fracture-toughness-based criteria. The applicability of the simple fracturing law is further confirmed from numerical modelling of crack propagation and coalescence problems with complex pre-existing cracks. Our results show that models with an appropriate resolution can simulate the crack path reasonably. Finally, the advantages of using the simple fracturing law are highlighted through multiple dynamic crack propagation and three-dimensional fracturing.

List of abbreviations

BEM	boundary element method
BMP	bonded particle models
CCNBD	cracked chevron notched Brazilian disc
CSTBD	cracked straight-through Brazilian disc
DDA	discontinuous deformation analysis
DEM	discrete element method
DLSM	distinct lattice spring model
EPFM	elastic plastic fracture mechanics
FDM	finite difference method
FEM	finite element method
FPZ	fracture process zone
HCFBD	holed-cracked flattened Brazilian disc
LEFM	linear elastic fracture mechanics
LSM	lattice spring model
NMM	numerical manifold method
PFC	particle flow code
PMMA	polymethyl methacrylate
PPC	Portland Pozzolana cement
RSD	relative standard deviation
SBFEM	scaled boundary finite element method
SCB	semicircular bending
SIF	stress intensity factor
SNDB	straight-notched disc bending

1. Introduction

Brittle solids containing cracks are thought to be highly risky for engineering applications. Cracks accelerate failure and add to the complexity of failure prediction, thus causing many disasters. For example, in the case of an eight-story residential building collapse in Bangladesh in 2013, it was reported that a crack was found on the concrete floor before the collapse (Than, 2013). However, humans make use of the induced crack propagation through rock mass in underground oil/gas reservoirs to extract resources. No matter on which aspects, disaster control or resource exploitation, understanding of crack propagation is essential. Therefore, research on crack propagation in brittle material is in demand.

Numerical experiments are favourable because they help foresee many results at low cost, thus providing guidance for practice.

* Corresponding author.
E-mail address: gaofeng.zhao@tju.edu.cn (G.-F. Zhao).

http://dx.doi.org/10.1016/j.ijsolstr.2017.04.024
0020-7683/

Numerical methods can be broadly grouped into two categories: continuum-based methods and discontinuum-based methods. The success of continuum-based methods is attributed to pioneering works including the proposals of the energy release rate by Griffith (1921); stress intensity factor (SIF) by Irwin (1957), who set up the crack propagation criterion in linear elastic fracture mechanics (LEFM); J-integral (Rice, 1968) in elastic plastic fracture mechanics (EPFM); and fracture process zone (FPZ) models (Bazant and Cedolin, 1979; Hillerborg et al., 1976). Popular continuum-based numerical methods (e.g., the finite element method (FEM), finite difference method (FDM), boundary element method (BEM), and numerical manifold method (NMM) often use the SIF as the most widely accepted criterion, which can be calculated by the J-integral, the stiffness derivative method (Parks, 1974), or methods based on nodal displacement near a crack tip (Fu et al., 2012). However, the calculation of the SIF in the presence of pre-existing cracks or near boundaries is inaccurate. Moreover, the SIF is difficult to determine in a non-homogeneous material, although solutions are found in functionally graded materials (Dolbow and Gosz, 2002; Rao and Rahman, 2003; Song and Paulino, 2006).

Unlike continuum models, discontinuum-based models use a bottom-up methodology and assemble the solid body with discontinuous elements. Because of that feature, these methods do not require special treatment for the formulation of elements near the discontinuities and can simulate complete detachment of material, which is difficult to obtain in continuum-based models with rock mass, ice plates, flow of granular materials, etc. (Lisjak and Grasselli, 2014). Because the development of high-performance computing alleviates the disadvantage of being computational expensive, discontinuum-based models have become favourable, especially in working with complex discontinuities and material heterogeneity. Compared with the continuum approach, the calculation of the SIF or energy release rate is not the essential intermediate step for simulating crack propagation, and the crack propagates when the strain or stress level excesses the threshold value between the discrete elements. The straightforward criteria are successful in simulating crack propagation using the discrete element method (DEM) (Cundall, 1971), bonded particle model (BMP) (Potyondy and Cundall, 2004) and discontinuous deformation analysis (DDA) method (Shi and Goodman, 1988). Lattice spring models (LSMs), which originated from Hrennikoff (1941), use natural failure of the springs between particles as the criterion. The earlier versions of LSMs (e.g. Beale and Srolovitz, 1988; Donzé and Magnier, 1995; Srolovitz and Beale, 1988) has a limitation of a fixed Poisson's ratio (i.e., 0.25 for three dimensions and 0.33 for two dimensions) (Zhao, 2017; Zhao, 2010). Later, the introduction of the shear spring broke that limitation, but LSMs still cannot represent the full range of Poisson's ratio (e.g. upper boundary of 0.25 for plane strain condition and 0.33 for plane stress condition (Zhao et al., 2012)).The distinct lattice spring model (DLSM) proposed by Zhao et al., (2011) used local strain calculation technique to consider the rotational effects instead of adding additional degree of freedom. It utilises the multi-body shear spring, allowing the model to represent diverse Poisson's ratios without violating the rotational invariance because the relative shear deformation is calculated from a particle cluster by using a local strain method rather than the shear displacement of two particles. Compared with conventional DEM, DLSM does not need to determine the micro-parameters because these parameters are directly derived from the macro-parameters. In addition, DLSM halves the degrees of freedom in DEM, thus reducing the computational cost. Because heterogeneity or high discontinuity in a material will have a significant influence on the crack trajectory (Cotterell and Rice, 1980), crack propagation by natural breakage of the springs seems to be more realistic and objective.

DLSM has been successfully used in crack problems (e.g. Gui and Zhao, 2015; Jiang et al., 2016) . However, the verification of this method in fracture mechanics is absent, and its capability in simulating crack propagation is questionable. This paper employs DLSM to investigate crack propagation in brittle material. The simple fracturing criteria based on spring deformation will be critically assessed. In addition, the fracture toughness is calculated for different particle sizes, and the relationship between critical SIF and spring failure is investigated. Finally, the validations and applications of this discrete particle model are briefly illustrated through quasi-static and dynamic examples.

The content in the paper is organised as follows: In Section 2, the algorithm of DLSM is briefly outlined. In Section 3, the relationship of the simple fracturing law and linear elastic fracture mechanics is investigated, including the correlation of spring deformation and SIF in Section 3.1, influence of particle size and fracture toughness in Section 3.2, and relationship between spring failure and critical stress intensity factor in Section 3.3. In Section 4, the validations and applications to crack propagation and coalescence are presented through quasi-static and dynamic fracturing with 2D and 3D examples. The paper ends with some conclusions and remarks.

2. DLSM algorithm

The distinct lattice spring model (DLSM) was proposed by Zhao et al., (2011). In DLSM, the lattice model is formed by linking the particles whose centre-to-centre distances are smaller than a threshold value. Accordingly, the particles with prescribed sizes are linked by a pair of springs, namely, a normal spring and a shear spring, in clusters (see Fig. 1a). The springs have a constitutive model as described in Fig. 1c. Either spring has an ultimate displacement (Un^* or Us^*) within which the springs obey Hooke's law and beyond which the particles will have only a contact bond with zero strength, which has been proved to be realistic in fracture pattern and this treatment is one of the advantages over FEM (Zhao and Khalili, 2012b). The normal spring was implemented in the classic lattice spring model. The normal unit vector $\mathbf{n}=(n_x,n_y,n_z)^{\mathbf{T}}$ is defined as pointing from particle i to particle j, linked by a bond. The normal deformation of the spring is defined as

$$\mathbf{u}_{ij}^{n} = \left(\mathbf{u}_{ij} \bullet \mathbf{n}\right)\mathbf{n} \tag{1}$$

where $\mathbf{n}_{ij}=\mathbf{n}_j-\mathbf{n}_i$is the relative displacement between two particles. Obeying Hooke's law, the normal force between the two particles is given as

$$\mathbf{F}_{ij}^{n} = \begin{cases} k_n \mathbf{u}_{ij}^{n} & \text{for } \mathbf{u}_{ij}^{n} < \mathrm{Un}^* \\ 0(\text{break}) & \text{else} \end{cases} \tag{2}$$

where k_n is the stiffness of the normal spring.

The major distinct feature of DLSM is that a shear spring is introduced to break the limitation in various Poisson's ratios in classic lattice spring models (Zhao et al., 2011). The shear spring is introduced to describe the multibody non-central interaction. The shear spring allows the model to represent diverse Poisson's ratios without violating the rotational invariance because the relative shear deformation is calculated from a particle cluster by using a local strain method rather than the shear displacement of the two particles, which is calculated as (Zhao et al., 2011)

$$\hat{\mathbf{u}}_{ij}^{s} = [\varepsilon]_{bond}\mathbf{n} - (([\varepsilon]_{bond}\mathbf{n}) \bullet \mathbf{n})\mathbf{n} \tag{3}$$

where$[\boldsymbol{\varepsilon}]_{bond}$ is the local strain of the connecting bond and is evaluated as the average of the linked particle strains $[\boldsymbol{\varepsilon}]_i$ and $[\boldsymbol{\varepsilon}]_j$, which are evaluated by a least square method (Zhao et al., 2011). The shear force between the two particles is given as

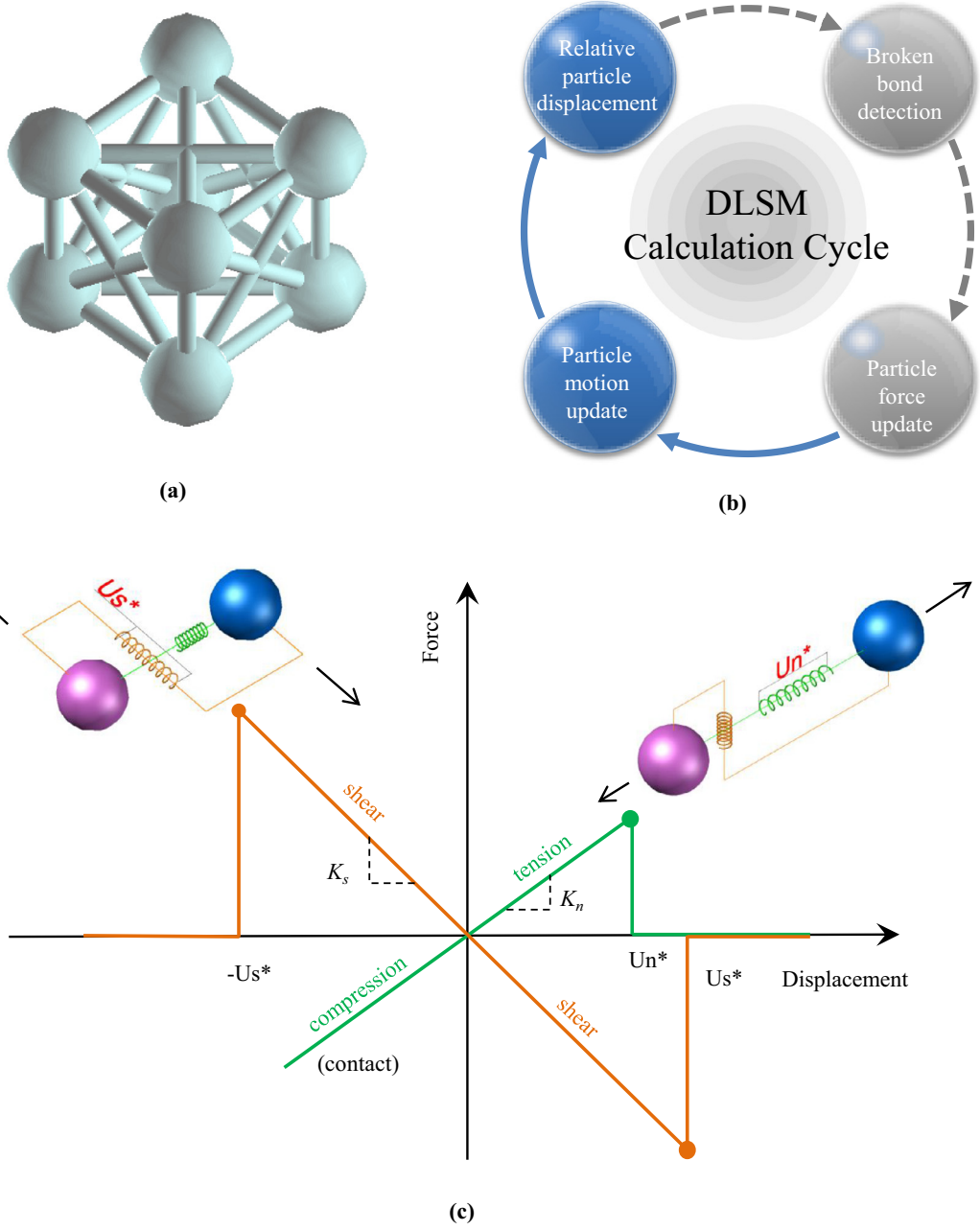

Fig. 1. (a) Schematic illustration of the normal spring and shear spring in DLSM. (b) The calculation cycle in DLSM. (c) The constitutive model of normal and shear springs.

$$\mathbf{F}_{ij}^{s} = \begin{cases} k_s \hat{\mathbf{u}}_{ij}^{s} & \text{for } \hat{\mathbf{u}}_{ij}^{s} < \text{Us}^* \\ 0(\text{break}) & \text{else} \end{cases} \tag{4}$$

where k_s is the stiffness of the shear spring. The Eqs. (2) and (4) make the fracture criterion in DLSM also as depicted in Fig. 1(c), and the ultimate displacements are calibrated through experiments. It is noted that they exist or disappear simultaneously in pairs (i.e. either spring's breakage will break the other spring). In DLSM, material is discretized into a group of particles linked through springs. The crack propagation, fragmentation and failure of solids are represented as the progressive failure of these springs. Therefore, in DLSM, the crack initiation in the model will be the first break of any spring, and crack extension is represented as a series of micro failure events (breakage of springs).

The relationships between micro-spring parameters (k_n and k_s) and macro-material properties (E and υ) are derived by Cauchy–Born rules and the hyperelasticity theory. The equations (Zhao et al., 2011) for k_n and k_s in the elastic domain are

$$k_n = \frac{3E}{\alpha^{3D}(1-2\upsilon)} \tag{5}$$

$$k_s = \frac{3(1-4\upsilon)E}{\alpha^{3D}(1+\upsilon)(1-2\upsilon)} \tag{6}$$

where α^{3D} is a microstructure geometry coefficient that can be obtained as

$$\alpha^{3D} = \frac{\sum l_i^2}{V_m} \tag{7}$$

where l_i is the original length of the ith spring, and V_m is the volume of the represented geometry model.

The motion equation (Zhao et al., 2011) of the lattice system, which consists of mass particles and springs, can be represented

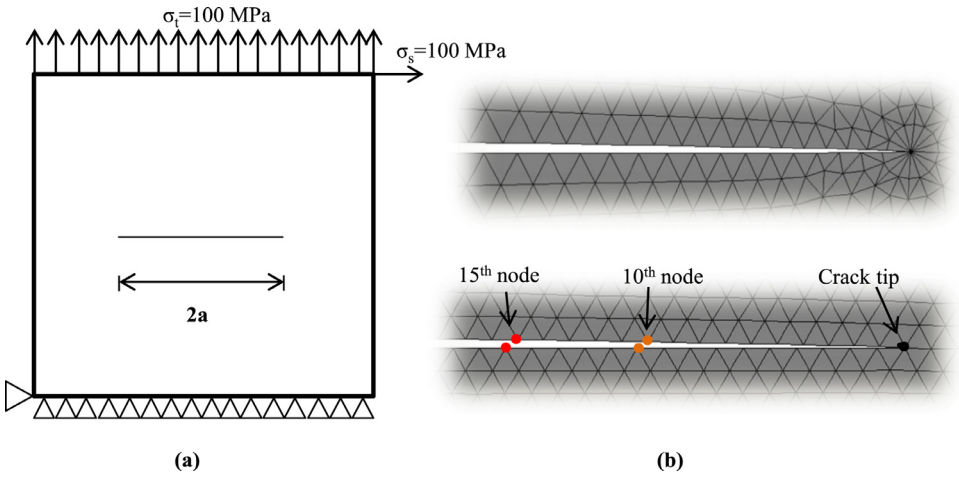

Fig. 2. (a) Loading schematics for evaluating a displacement extrapolation method. (b) ANSYS model with singular elements at the tip and with regular meshes.

as

$$[\mathbf{K}]\mathbf{u} + [\mathbf{C}]\dot{\mathbf{u}} + [\mathbf{M}]\ddot{\mathbf{u}} = \mathbf{F}(t) \tag{8}$$

where $\mathbf{u}$ represents the vector of particle displacement, [**K**]is the stiffness matrix, [**M**]is the diagonal mass matrix, [**C**]is the damping matrix, $\mathbf{F}(t)$is the vector of external force, $\dot{\mathbf{u}}$ is the particle velocity, and $\ddot{\mathbf{u}}$ is the particle acceleration. In DLSM, the explicit central finite difference method is used to solve Eq. (8).

The calculation cycle is shown in Fig. 1b. The relative particle displacement can detect any broken bonds and update the forces acting on the particles. The acting forces promote the movement of particles. With the calculated particle velocity, the relative particle displacement is recalculated for the second loop. The particle velocity is obtained as

$$\dot{\mathbf{u}}^{(t+\Delta t/2)} = \dot{\mathbf{u}}^{(t-\Delta t/2)} + \ddot{\mathbf{u}}\Delta t \tag{9}$$

where Δt is the time step, $\dot{\mathbf{u}}^{(t+\Delta t/2)}$ is the particle velocity at $t + \Delta t/2$, $\dot{\mathbf{u}}^{(t-\Delta t/2)}$ is the particle velocity at $t - \Delta t/2$, and $\ddot{\mathbf{u}}$ is the acceleration of the particle, which is calculated from Newton's second law as

$$\ddot{\mathbf{u}} = \frac{\sum \mathbf{F}^{(t)}}{m_p} \tag{10}$$

where m_p is the particle mass, and $\sum \mathbf{F}^{(t)}$ is the sum of contact forces acting on the particle including applied external forces. Eventually, the new displacement of the particle is calculated as

$$\mathbf{u}^{(t+\Delta t)} = \mathbf{u}^{(t)} + \dot{\mathbf{u}}^{(t+\Delta t/2)}\Delta t \tag{11}$$

where $\mathbf{u}^{(t+\Delta t)}$ is the displacement at the next time step, and $\boldsymbol{u}^{(t)}$ is the displacement at t.

For static problems, mechanical damping (Zhao et al., 2011) is used, which can be expressed as

$$\dot{\mathbf{u}}^{(t+\Delta t/2)} = \dot{\mathbf{u}}^{(t-\Delta t/2)} + \left\{\sum \mathbf{F}^{(t)} - \chi\left|\sum \mathbf{F}^{(t)}\right|\mathrm{sgn}\left(\dot{\mathbf{u}}^{(t-\Delta t/2)}\right)\right\}\frac{\Delta t}{m_p} \tag{12}$$

where χ is the damping constant.

The advantages of DLSM for crack propagation in brittle material are as follows. First, the constitutive model of the microstructure is easy to implement, so the result from the simulation is easy to interpret. Moreover, the calibration is simpler because fewer parameters are required than in other discontinuum-based models, e.g., particle flow code (PFC). Second, because of its meshless and rotationally invariant nature, a very complex model with pre-existing cracks can be built. In other words, there is no limitation on the geometry of the model. Third, parallelization of DLSM gives this model high computational performance which is available on both central processing unit (CPU) (Zhao et al., 2013) and graphics processing unit (GPU) (Zhao and Khalili, 2012a).

3. DLSM for crack propagation

3.1. Correlation of spring deformation to SIF

DLSM uses a fracture criterion simply based on spring deformation, so the verification of this criterion is necessary. To illustrate, a 100 mm × 100 mm square model with a central pre-existing line crack of length 2a is designed in Fig. 2a. The bottom is fixed in both the X and Y directions. Two layers of particles are used along the thickness, and the model is assumed to be in the plane stress condition. Two types of static stress (a normal stress and a shear stress) are applied to the top surface, and the model adopts mechanical damping to achieve quasi-static loading. To evaluate the stress state of the current fractured model, according to LEFM, the SIF at the crack tips is of greatest interest. The FEM-based simulator ANSYS is used as a tool in this study as it can accurately calculate the SIFs (e.g. by meshing with singular elements near the crack tip or using J-integral), which provide good references. In DLSM or other meshless models, the displacement extrapolation method (Chan et al., 1970) can be used. The simplest form is linear extrapolation in which at least two sets of node displacements are required. To decide which sets to use, two models are meshed in ANSYS, one with singular elements at the tip and one with all equal-sized triangular elements (refer to Fig. 2b). The model with equal-sized elements has the nodes evenly aligned such that the nodes' alignment along the crack faces is similar to that in DLSM. The node displacements are recorded to calculate the apparent stress intensity factors (K^*) of mode I and mode II using Eqs. (13) and (14).

$$K_I* = \sqrt{\frac{2\pi}{r}} \times \frac{G}{1+\kappa} \times V \tag{13}$$

$$K_{II}* = \sqrt{\frac{2\pi}{r}} \times \frac{G}{1+\kappa} \times U \tag{14}$$

where r is the distance from the crack tip, G is the shear modulus, $\kappa = (3 - \upsilon)/(1 + \upsilon)$ in the plane stress condition, and V and U are the relative displacements of the corresponding nodes in the normal and shear directions, respectively. Different sets of nodes are tried for the calculation of K^* to match the results obtained from

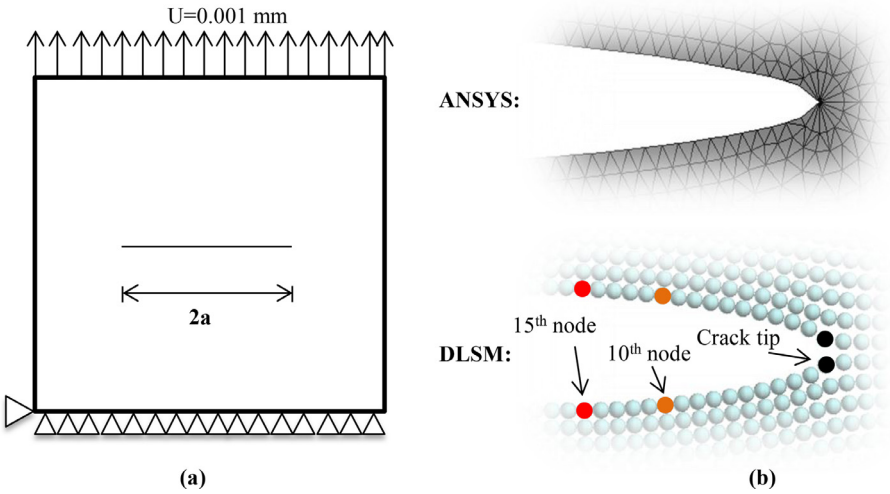

Fig. 3. (a) Loading schematics under pure tension. (b) ANSYS model with singular elements at the tip; DLSM model using the displacement extrapolation method or directly using $U_{cod\text{-}tip}$.

the model with singular elements. However, too many choices can be selected for linear extrapolation. For example, in a crack with a half crack length of 20 mm with 1 mm mesh size, there are 190 combinations for different results. We define a ratio of the distances from crack tip to the farther node and closer node. The ratio cannot be too large because the second (farther) node may become unavailable in the models with few nodes, and cannot be too small because the two nodes should represent the whole crack faces. Therefore, an intermediate ratio of 1.5 is determined. The errors compared to FEM solutions for all possible combinations on a model with crack length of 40 mm are calculated and plotted in the Appendix Fig. A1. The results are based on three resolutions of the mesh, i.e. 0.5 mm, 0.8 mm and 1 mm. It is noted that the first node being the 10th node generate the best results. Therefore, the two datasets adopted for linear extrapolation are the displacements of the 10th and 15th nodes counting away from the crack tip along each crack face, as depicted in Fig. 2b. This method has also been verified by rotating the pre-existing crack by different angles, and the differences with FEM are less than 5% (refer to the results in Table A1 in Appendix). The two point linear extrapolation strategy with Eqs. (13) and (14) is assumed to be applicable in DLSM whose particles along the crack faces are evenly distributed as well. It needs to be mentioned that the crack propagation is not controlled by SIFs in DLSM, and the purpose of calculating SIFs is to explore the connection to LEFM and reason why discrete models (such as LSM) are able to be used for crack propagation.

The validation has been performed in DLSM models with 0.5 mm and 1 mm in particle size and with five different pre-existing crack lengths (2a = 40 mm, 50 mm, 60 mm, 70 mm and 80 mm) under a pure tensile (mode I) load (refer to Fig. 3a). The comparison is made between ANSYS's results with singular elements and DLSM's results with the aforementioned strategy (refer to Fig. 3b). The calculated results indicate that the difference in K_I values is within only 2% (refer to Appendix Table A2). This means that under the same criterion as the SIF, DLSM can provide similar results as LEFM. To illustrate, the calculated SIFs in mode I (K_I) are plotted as dimensionless values corresponding to their maximum values in Fig. 4. In addition, the normal spring deformation between the two particles at the crack tip (named $U_{cod\text{-}tip}$) are also recorded and plotted on the same graph. It should be mentioned that $U_{cod\text{-}tip}$ has a closer match to the trend of K_I from the FEM analysis in Fig. 4, which indicates that this value has a strong correlation with the SIF, which is regarded as the most important parameter in LEFM. Therefore, it is deduced that $U_{cod\text{-}tip}$ has the

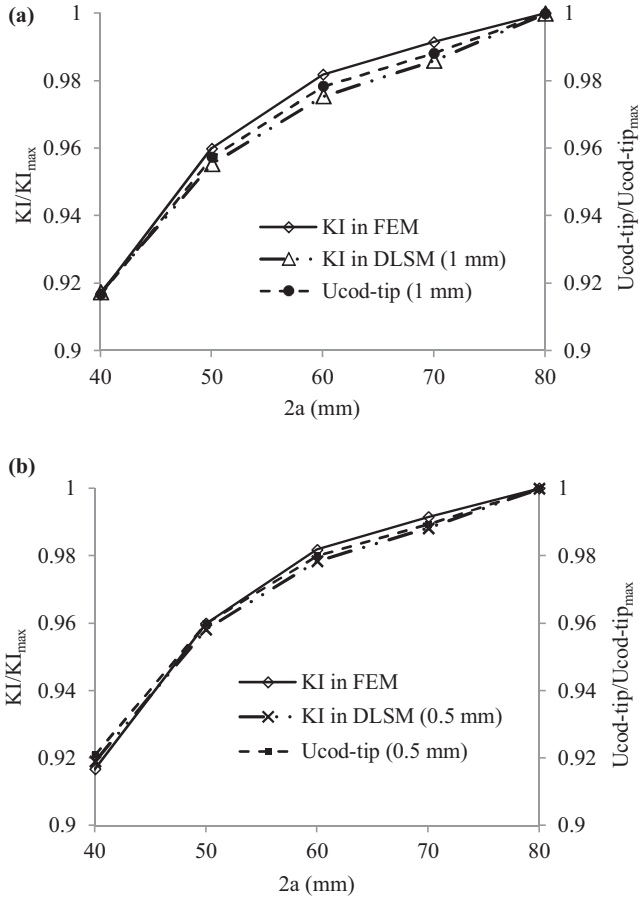

Fig. 4. Results of the calculated SIF and normal spring deformation between the two particles at the crack tip ($U_{cod\text{-}tip}$). (a) particle size = 1 mm (b) particle size = 0.5 mm.

potential to be used to predict crack failure in DLSM. In other words, the spring deformation criterion may replace the conventional criterion from fracture mechanics, which requires calculating the stress intensity factor. This could be one reason, to some extent, why discrete particle models could be computationally more

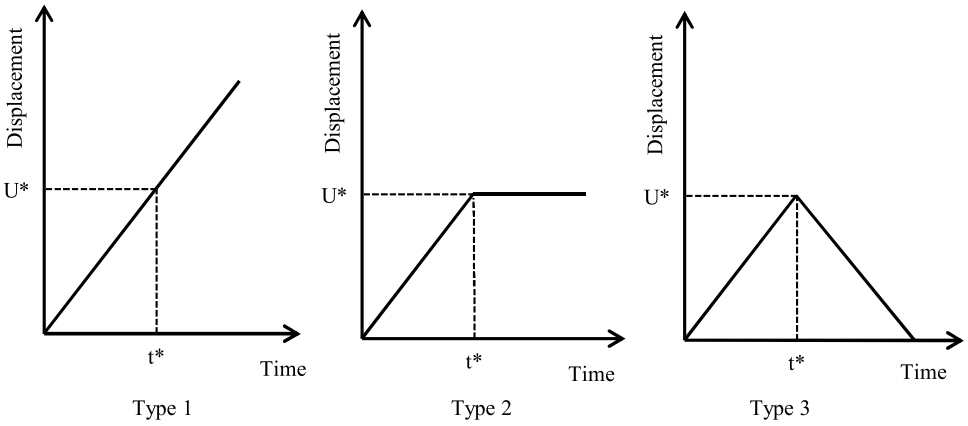

(a)

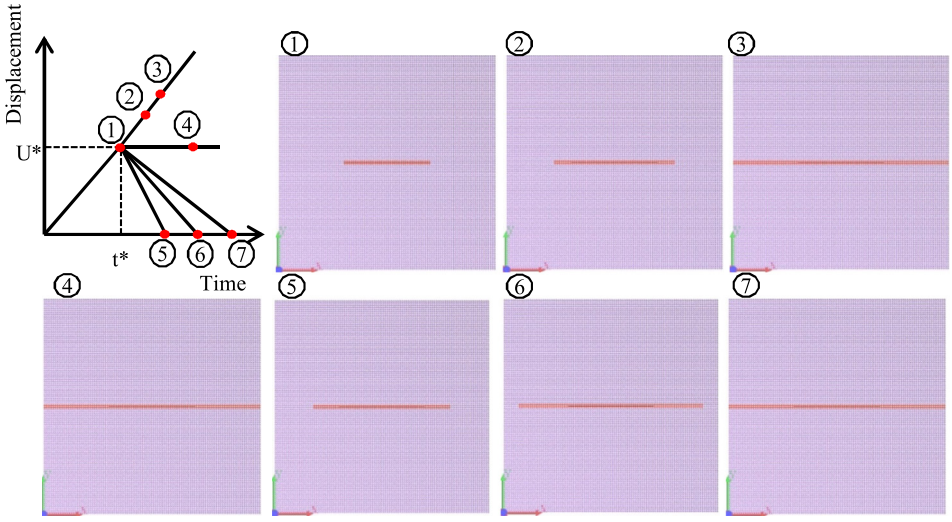

(b)

Fig. 5. Mode I crack initiation, propagation and arrest tests.(a) three loading types (b) crack path in different states.

efficient than continuum-based models in fracture detection near crack tips.

To verify that such a simple criterion can be used in fracture scenarios for simulating crack initiation, propagation and arrest, pure tensile stress as remote loading is applied again in the same model as a dynamic case in which the mechanical damping is removed. To control the total energy in the system, the displacement control method is used. The displacement control occurs in two stages. In the first stage, the model is pulled under a remote uniform velocity to a displacement of U*, which is just before the activation of crack initiation (see Fig. 5a). In the second stage, there are three types of loading: (1) continuing to load with the same speed, (2) fixing the top boundary at the same position and (3) unloading with a selected speed. In Fig. 5b, 7 points are picked, and their crack states are correspondingly illustrated. In type 1 loading, the crack propagation continues to transmit after the displacement of U*. It should be mentioned that a moderate speed is selected to avoid branching so that the crack propagates in the pure opening mode throughout the whole process. In loading type 2, it is interesting to note that the crack propagation still continues and runs through the model rather than stop (see point 4 in Fig. 5b). This indicates that there is still high energy remaining in the model although no extra energy is added to the system (i.e., the displacement is kept constant). To remove the redundant energy for further propagation, negative work is applied to the model by reducing the displacement to zero in loading type 3, in which the crack arrest is captured. Comparing point 5 and point 6, it is also noted that with increasing unloading rate, the crack is arrested with a smaller crack length, whereas there is still a crack stoppage failure with the insufficient unloading rate at point 7.

The crack criterion in DLSM is simple, but it can successfully show the ability for simulating crack initiation, propagation and arrest. Moreover, simple numerically implemented linear loading and unloading by remote control has also successfully affirmed the phenomenon that in a material with a pre-existing crack, the unstable crack may still propagate after the loading is removed or even negatively applied, which is an essential understanding for crack propagation control in certain engineering practice. Because failure of brittle material is unstable and crack propagates rapidly without increase in applied stress. In addition to the building collapse in Bangladesh in the introduction, another example of the sudden crack failure in on Schenectady T2 tanker in 1943 in which one of the reasons is on low temperature that embrittles steels (The Welding Institute, 2017). Our simulation results indicated that the crack propagation is a progress of energy release and brittle fracture easily causes catastrophic event.

In this section, only K_I in DLSM is considered. But it needs to be mentioned that K_{II} can also be calculated by Eq. (14) with similar

Table 1
Configurations of models in DLSM and results of fracture toughnesses.

Test type	Dimension (mm)	*Fracture toughness (1 mm)	*Fracture toughness (0.5 mm)	*Fracture toughness (0.25 mm)
SCB	$D=30, t=12$, $a=7.5$,Span $=24$	2.00	1.30	1.15
CSTBD	$D=30, t=12$, $2a=13.5$	2.67	1.62	1.01
CCNBD	$D=30, t=12, a_0=2.6775$, $a_1=8.8875$	2.73	1.55	1.13
HCFBD	$D=30, t=12$, $2a=15$, $r=3$	2.22	1.40	1.14
	SD	0.35	0.14	0.07
	RSD (%)	14.61	9.67	6.24

(*unit: MPa.m$^{0.5}$)

procedures. However, we found that the micro tensile failure can reproduced both fracture patterns in mode I and mode II from our physical tests and tests from the literature, which will be described in Section 3.3.

3.2. Influence of particle size on fracture toughness

Fracture toughness is an indication of the amount of stress required to propagate a fracture and is regarded as the key parameter in materials containing a crack. In conventional fracture mechanics, a material has a fracture toughness value for each mode of loading, i.e., subject to tension, shear and tear. Many testing methods are designed to obtain this parameter. For example, the mode I fracture toughness can be determined through a cracked straight-through Brazilian disc (CSTBD) test (Atkinson et al., 1982), cracked chevron notched Brazilian disc (CCNBD) test (Fowell, 1995), semi-circular bending (SCB) test (Aliha and Ayatollahi, 2011), three-point round bar test (Backers, 2005), double-cantilever beam test (Davies et al., 1998), holed-cracked flattened Brazilian disc (HCFBD) (Wang et al., 2010), etc. However, for the same type of material, the fracture toughness was reported to vary under different testing methods (Rao et al., 2003; Theocaris and Papadopoulos, 1984). For example, Tutluoglu and Keles (2011) conducted mode I fracture toughness tests on andesite and marble using the SCB, CCNBD and straight-notched disc bending (SNDB) methods, and the variation of fracture toughness was noted. They explained that the variation was caused by the specimen geometry, i.e., the size of the fracture process zone (FPZ). However, their experiment did not use homogeneous material, so it may be possible that a significant portion of the inconsistency was due to the heterogeneity of the material, apart from the geometry or the testing method itself.

Actually, we consider that the inconsistency is influenced by the intrinsic length-scale of the microstructure of the material. To verify this hypothesis, models at three different resolutions (particle sizes of 1 mm, 0.5 mm and 0.25 mm) are used in homogeneous DLSMs for four testing methods (SCB, CSTBD, CCNBD and HCFBD). The simulation material is with Young's modulus of 4.1 GPa, a Poisson's ratio of 0.19 and their geometries are listed in Table 1. The dispersion of K_{IC} among the four testing methods is described using the relative standard deviation (RSD). The RSDs for the three particle sizes are plotted in Fig. 6 for comparison. It shows that the RSD decreases as the particles become finer. Therefore, it is predicted that with a sufficient decrease in particle size, the variance will approach zero. When the particle size becomes infinitesimal, which is equivalent to the assumptions behind the continuum-based models, the fracture toughness will be a constant regardless of the geometry. Nevertheless, in real materials, atoms or molecules will form a certain mixture that has intrinsic length-scale of the microstructure. For example, in sandstone, the particles can be observed by the naked eye, so it is impossible to obtain invariant fracture toughness with different testing methods. However, the particle-based model can reproduce the variance by selecting a proper simulation particle size so that the intrinsic length-scale of the microstructure can be deduced when the degree of variance is known.

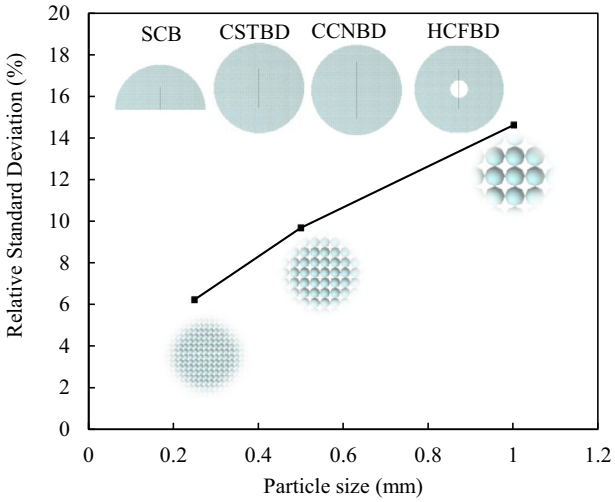

Fig. 6. Relative standard deviation among the fracture toughness tests. *Un** for models with diameter of 0.25 mm, 0.5 mm and 1 mm are 2.927e−3 mm, 5.854e−3 mm and 11.708e−3 mm, respectively.

In conclusion, because the fracture toughness from the tests is not invariable, its use as a fracturing criterion index in numerical modelling is questionable. Moreover, DLSM reveals that at least a significant portion of the inconsistency is related to the intrinsic length-scale of the microstructure in the material.

3.3. Relationship between the spring failure and critical stress intensity factors

SCB tests can be used for different fracture modes by varying the inclination angle β (see Fig. 7). The critical values of mode I and mode II stress intensity factors are calculated in components by Eqs. (15) and (16), respectively:

$$K_{If} = \frac{P_{cr}}{2Rt}\sqrt{\pi a}Y_I \tag{15}$$

$$K_{IIf} = \frac{P_{cr}}{2Rt}\sqrt{\pi a}Y_{II} \tag{16}$$

where Y_I or Y_{II} is the dimensionless SIF for mode I or II and is a function of a/R, s/R and β; $a$is the notch length; R is the radius of the semicircle; s is half the distance between two point supports at the bottom; and t is the thickness of the sample. Pure mode I corresponds to $\beta=0°$, and the pure mode II failure appears at $\beta=54°$ with $\alpha/R=0.35$ and $s/R=0.5$ according to Ayatollahi and Aliha (2007).

According to the aforementioned geometrical ratios, three DLSM models are built for mode I fracture ($\beta=0$), mixed mode fracture ($\beta=30°$) and mode II fracture ($\beta=54°$). The SCB experiment on sandstone and granite were also conducted using Shi-

Table 2
Material properties of rock used in SCB test.

	Origin	Density (g/cm^3)	E* (GPa)	σ_c*(MPa)	σ_t*(MPa)
Sandstone	Wuding county, Yunnan,China	2.21	9.8	71.4	3.7
Granite	Zhuozhou city, Hebei, China	2.73	31.7	151.3	7.3

(*Young's modulus E and compressive strength σ_c are from uniaxial compressive strength test and the tensile strengths σ_t are from Brazilian tensile strength tests)

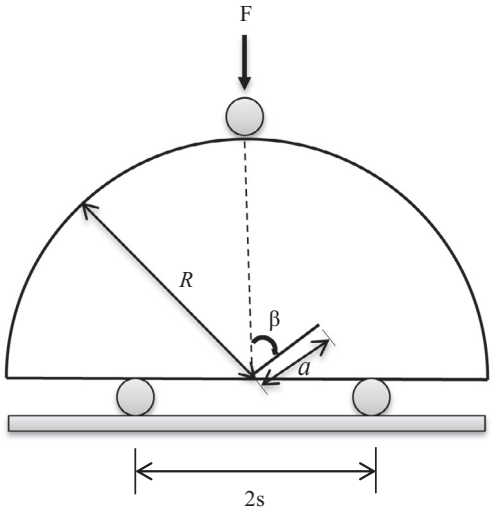

Fig. 7. Set-up of SCB test.

Table 3
Configurations of SCB on Johnstone selected from Lim et al., (1994a) and Lim et al., (1994b).

β	a (mm)	D (mm)	t (mm)	F_{peak} (kN)
0	16.4	95	19.8	0.187
0	16.4	95.9	20.3	0.193
0	16.7	95.1	19.7	0.183
0	16.9	95.9	20.4	0.235
30	16.3	95.9	20.6	0.268
30	17.7	95.8	20	0.236
30	16.5	95.9	19.8	0.211
30	16.7	95.9	19.9	0.212
54	16.6	95.8	18.5	0.346
54	16.9	96	19.3	0.384

madzu AGSH5KN universal tester. The specimens are 50 mm in diameter and 25 mm in thickness, and the pre-existing crack geometry follows the aforementioned ratios. The material properties obtained from mechanical tests are shown in Table 2. The DLSM simulation results are in reasonable agreement with the experimental fracture patterns in Fig. 8. However, only the normal spring is used as a fracturing criterion in the above examples; i.e., no shear spring breakage is allowed, but the crack path is still well simulated even for a pure mode II crack. To investigate the effectiveness of this simple fracturing law only by normal spring, the experiment on SCB specimens made of Johnstone in Lim et al. (1994a) and Lim et al. (1994b) is employed. The only failure parameter Un^* is calibrated by the mode I fracture toughness test on SCB specimen. Johnstone is a synthetic rock purported to be homogeneous and isotropic (Lim et al., 1994a). To be consistent, only the experimental data obtained with respect to $s/R = 0.5$ and $a/R = 0.35$ are utilized (refer to Table 3). First, DLSM is calibrated to match the mechanical behaviour of Johnstone. Lim et al. (1994a) provided a typical load-displacement curve of SCB, and its slope is used to calibrate the Young's modulus and the averaged peak value (about 0.2 kN) for mode I tests from deduction is used to calibrate Un^* (see Fig. 9). Using the same micro-parameter, DLSM simulated the fracture in mixed mode and mode II. The experimental data and simulated results are summarized in Fig. 10a. A perfect match is observed, which affirms that the simple fracturing law only depended on normal spring can be used in mixed mode and even mode II failure. This indicates that the macro-fracture behaviour could be a result of the accumulation of micro-normal spring failure only. Thus, the number of parameters for crack detection is reduced to only one in DLSM, whereas three intensity factors are required to be assessed in LEFM.

The same approach is also applied to sandstone and granite. The comparisons to the DLSM results are shown in Fig. 10b and c. It is observed that the two curves diverge but are still reasonably similar in trend. The divergence may be attributed to the heterogeneity of the rock because it is not as homogenous as the synthetic Johnstone: the mix of minerals can be observed at the sur-

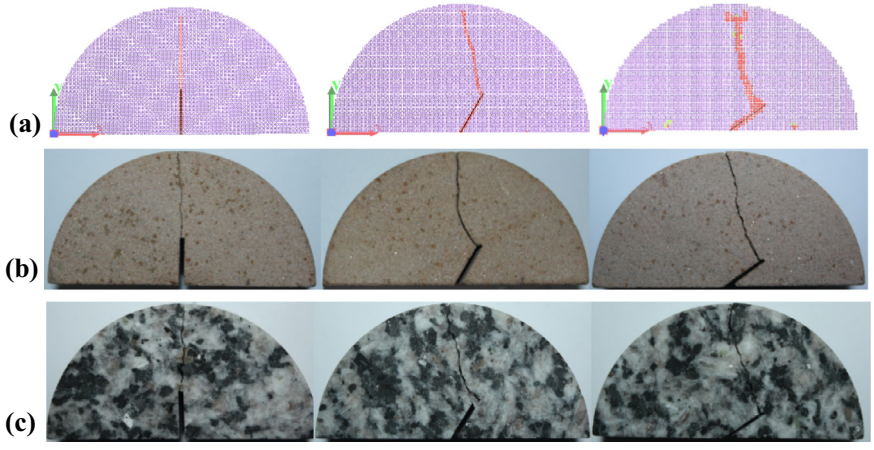

Fig. 8. Crack paths under different fracture modes in (a) DLSM (b) sandstone (c) granite; The crack path in DLSM is a result of successive failure of springs induced by normal springs only.

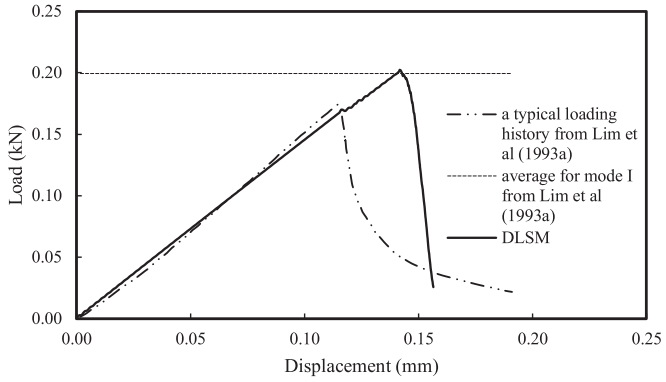

Fig. 9. Load-displacement curves for the specimen and model fractured in mode I.

face. Therefore, the heterogeneity is applied to the models using the single-parameter controlled Weibull distribution which is

$$f(\lambda) = \mathbf{m}\lambda^{\mathbf{m}-1}e^{(-\lambda^{\mathbf{m}})} \tag{17}$$

where λis the scaled parameter that described the property of the material and **m** is the shape factor which implies that the properties of particles will be within a narrow range close to the mean value for higher value of **m**. In another word, the larger value of **m** indicates more homogeneous material (refer to Fig. 10d). The strength of the material is governed by the ultimate spring deformation Un^* whose values of every normal spring is individually assigned as

$$Un^* = \lambda Un_0^* \tag{18}$$

where Un_0^* is the average ultimate normal spring deformation in the model. It is found that the incorporation of Weibull distribution can revise the model toward the experimental results, e.g. the curve in Fig. 10b with $\mathbf{m} = 5$ lies close to the experimental one for sandstone. However, it is still unreasonable for the granite. This is because the micro-composition of the granite cannot be ignored

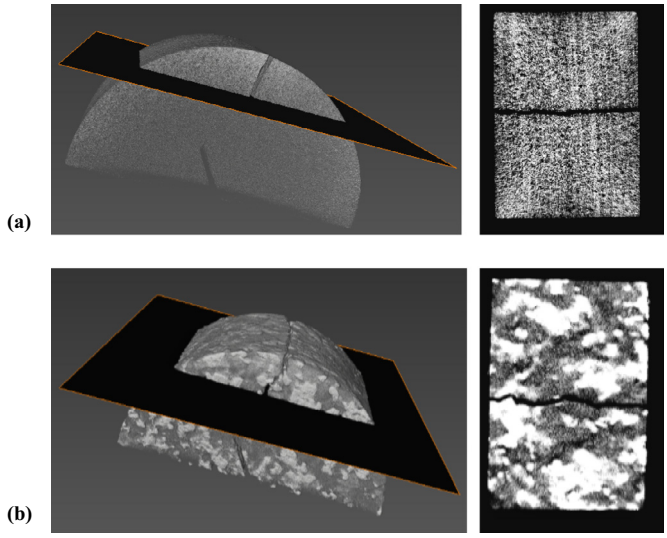

Fig. 11. Top view of the crack along the thickness in SCB specimens under X-ray CT for (a) sandstone (b) granite.

and the Weibull distribution cannot be simply used to represent the heterogeneity. The micro-scale X-ray CT images in Fig. 11 show a relatively straight crack path across the thickness in sandstone but a rough path for granite that skirts around some tough grains. To realistically simulate the granite, the microstructure of the rock must be included in the numerical model in the specific location, which could be accomplished with the aid of CT scanning.

The validations thus far affirm that the simple fracturing law by normal spring failure can be used to model crack propagation in the mixed mode. It is indicated that the macro-failure mechanism is not interrelated one-to-one to the micro-failure modes in this discrete particle model.

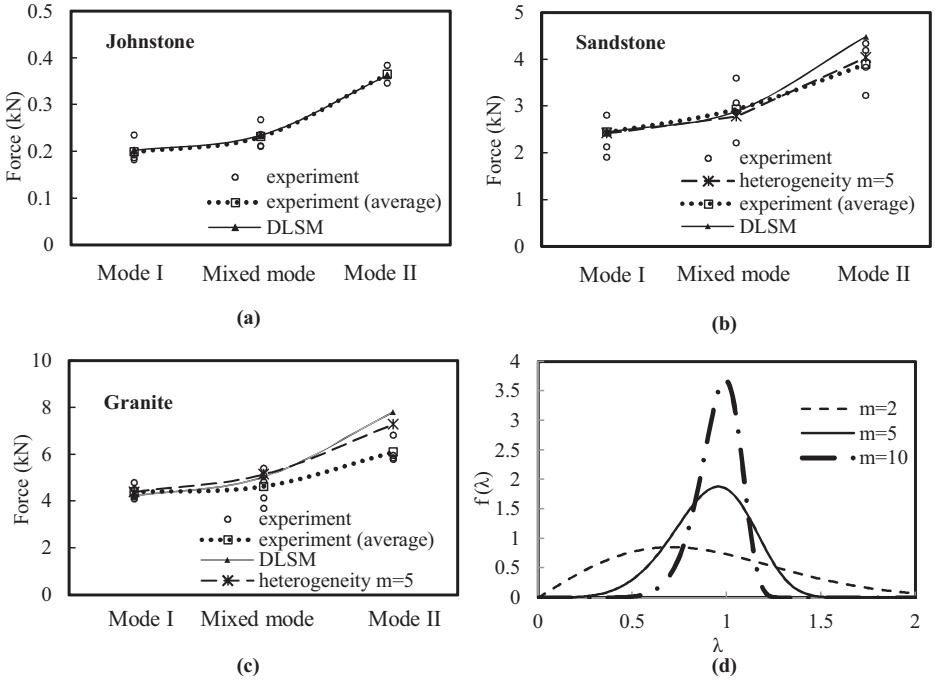

Fig. 10. Comparisons of the DLSM models with experiments on SCB specimens made of (a) Johnstone (b) sandstone (c) granite. Particle size = 1 mm, Un^* for (a),(b) and (c) are 0.0068 mm, 0.023 mm and 0.021 mm, respectively. (d) Weibull distribution of the scaled parameter with different values of shape factor **m**.

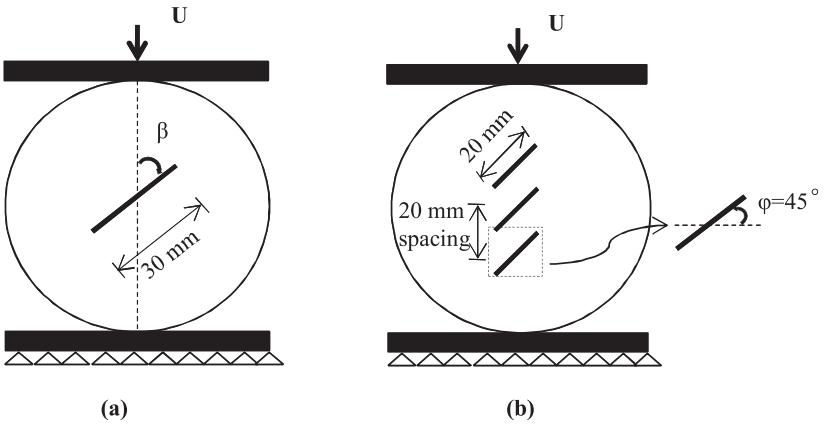

Fig. 12. Loading conditions in DLSM.(a) Single notched disc with inclination angle β. (b) Multiple notched disc with relative angle $\varphi = 45°$.

4. Validation and applications

Further validation of the simple fracturing law will be conducted on quasi-static and dynamic examples in this section. Multiple pre-existing cracks will be applied to discs for the study of crack propagation and coalescence under quasi-static loading. Dynamic loading sceneries will be studied in perforated plates in 2D and a part of a sphere in 3D.

4.1. Quasi-static crack propagation

DLSM is used to simulate mixed mode crack propagation in a central notched Brazilian disc (CNBD) test conducted by Haeri et al. (2014). Their specimens were prepared from a mixture of Portland Pozzolana cement (PPC), fine sands and water. The material properties set in DLSM are based on Haeri et al. (2014): a Young's modulus of 15 GPa, a Poisson's ratio of 0.21, and a Brazilian tensile strength of 3.81 MPa. The model is a disc 100 mm in diameter in the plane stress condition. A pre-existing crack is designed with different inclination angles β with respect to the loading direction (see Fig. 12a).

In the simulation, the loading board is controlled with a constant speed. The particle size in DLSM is primarily chosen to be 1 mm in diameter with 7860 particles as its resolution is enough to produce satisfied crack patterns. However, it should be noted that the particle size in DLSM is much larger than the CNBD specimens made of cement from Haeri et al., (2014). The purpose is to reduce the computational time and replace the complex molecular potential function with a simple spring constitutive law. Fig. 13 shows

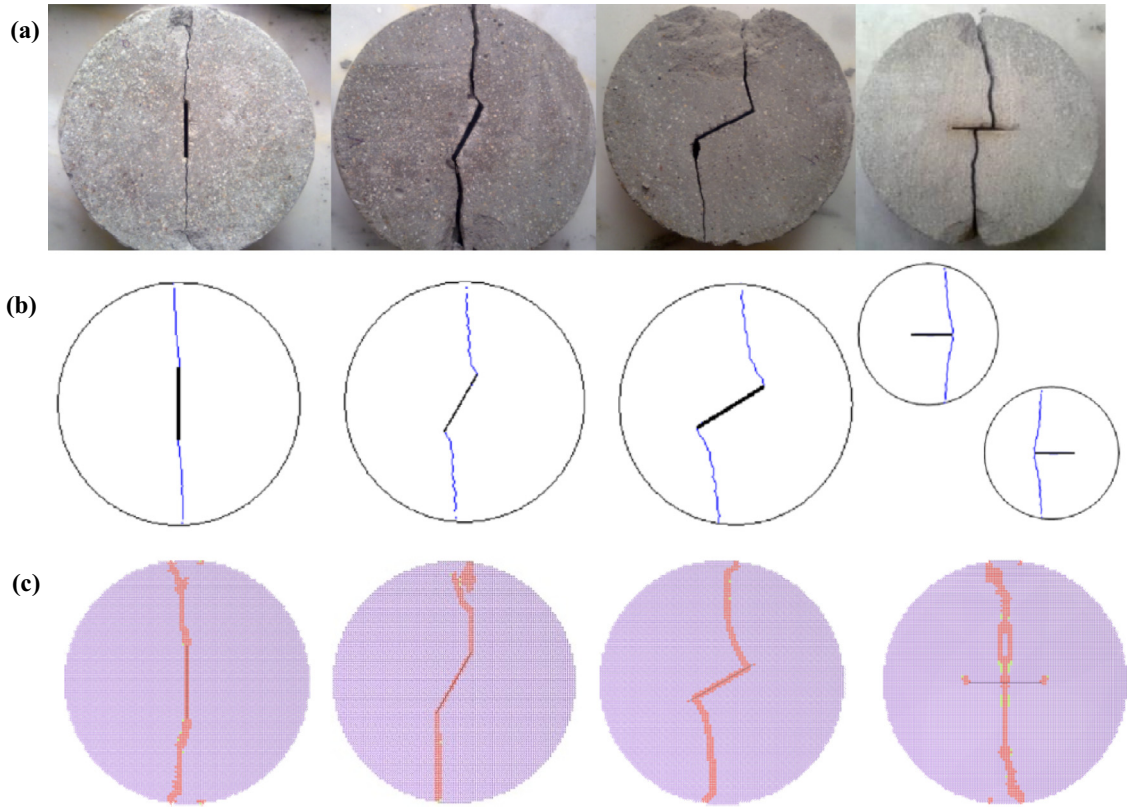

Fig. 13. Comparison of the results from experiment, BEM and DLSM with inclination angles of 0 °, 30 °, 60 °, 90 ° (a) Experiment (Haeri et al., 2014) (b) Results from BEM simulation (Haeri et al., 2014) (c) Results from DLSM with particle size = 1 mm, $Un^* = 2.54e{-}4$ mm.

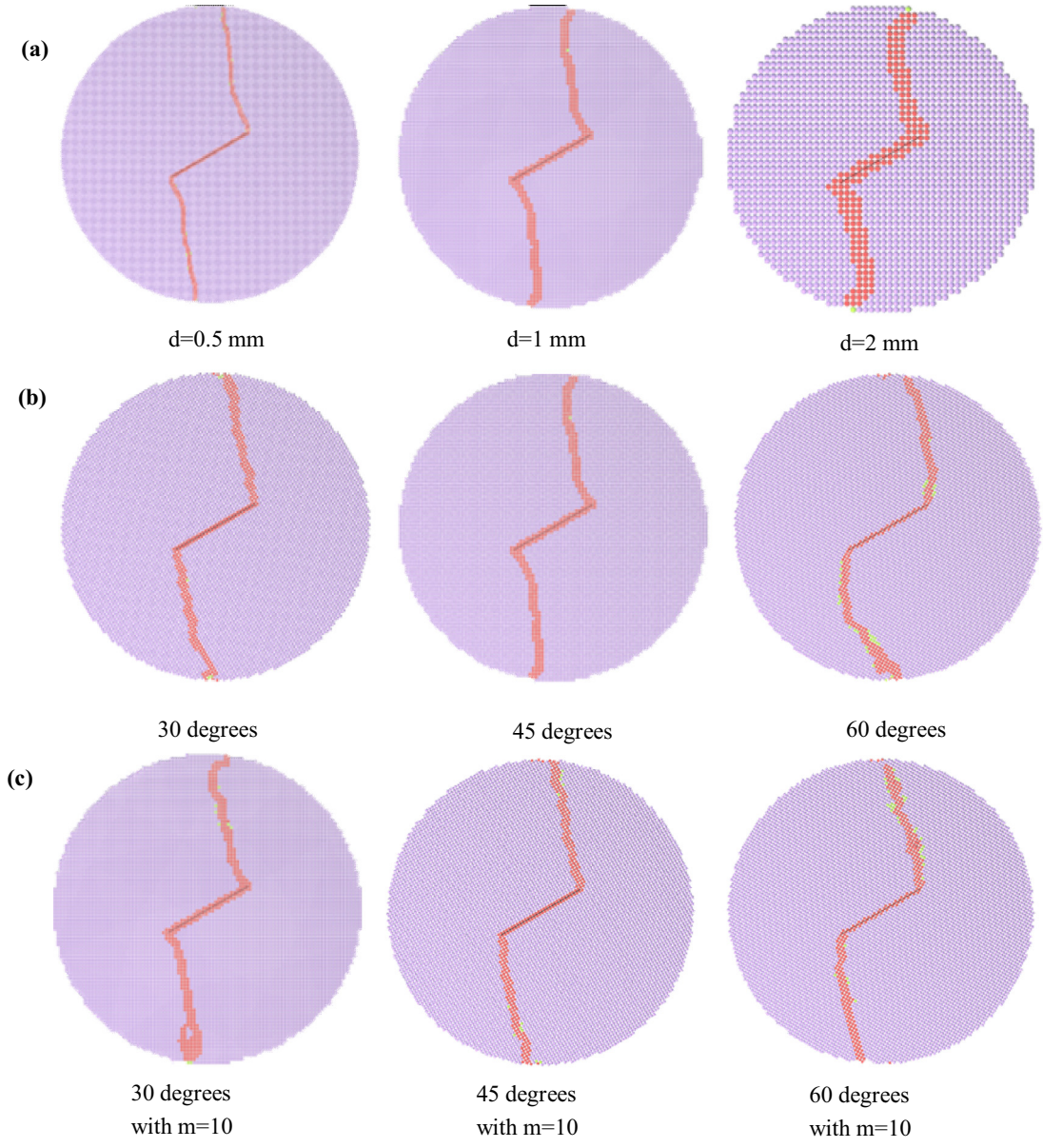

Fig. 14. Results after changes of simulation parameters in DLSM. (a) Simulation with different particle sizes. (b) Simulation with different particle alignments (c) Simulation with heterogeneity. For those whose particle sizes are not mentioned, particle size = 1 mm, $Un^* = 2.54e{-}4$ mm.

results from the experiment, boundary element method (BEM) and DLSM for four inclination angles (0°, 30°, 60° and 90°). It can be shown that DLSM can closely match the results from the experiment. In the first three cases, the cracks initiate at the tip of the notch, and the wing cracks propagate towards the maximum loading direction. However, when the inclination angle increases to 90°, the crack initiates from the centre of the specimen and diverges to the two loading boundaries. In comparison, the simulation by BEM in Haeri et al., (2014) always started the crack at either side of the notch tip, which is less realistic. Models with two different sizes (0.5 mm and 2 mm in diameter) are also chosen to examine the size effect on the crack pattern (Fig. 14a). The crack pattern tends to be slim when the particle size decreases. In other words, the crack grows in a more precise path with smaller particles (closer to PPC particles), which is more consistent with the experiment. However, even with a particle size of 2 mm, DLSM still produces a reasonable fracture pattern. In addition, the influence of the particle alignment direction is investigated. In the DLSM default model, the particles are stacked layer by layer, which is a horizontal alignment. Simulations are also run when the alignment tilts to 30°, 45° and 60° (Fig. 14b). It is found that the particle alignment has an influence on the wing crack curvature but not much influence on the general pattern. Moreover, the heterogeneity is applied with the Weibull distribution shape factor $\mathbf{m} = 10$. The crack paths illustrated in Fig. 14c indicate that the influences of the particle alignment angle are minified by adding the heterogeneity. Thus, through these simulations, DLSM has shown its strong flexibility in simulating crack propagation.

The crack coalescence is simulated by multi-crack CNBD testing, which is used for comparison with the experiment by Haeri et al. (2015), whose experimental material was the same as that of Haeri et al. (2014). In the multi-crack CNBD testing, parallel pre-existing cracks lay at 45° with a 20 mm centre-to-centre distance between the cracks (see Fig. 12b). There are four types of CNBD (see Fig. 15): those with two cracks, three cracks, four cracks and five cracks. The key observations are summarized as follows. First, the cracks initi-

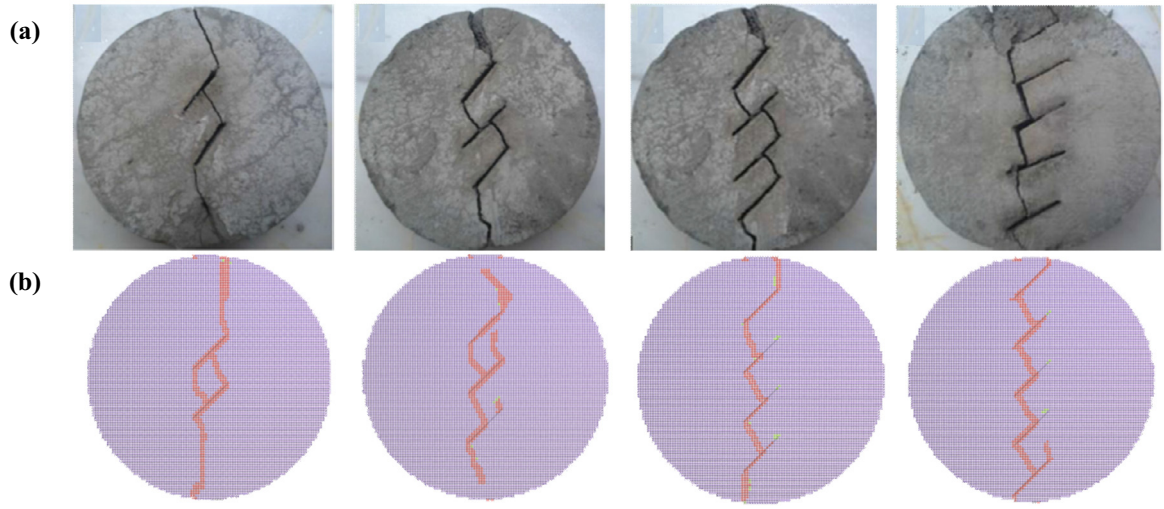

Fig. 15. Experimental and simulation results with multiple-notched CNBD. (a) Experimental results (Haeri et al., 2015) (b) Simulations from DLSM. Particle size = 1 mm, Un^* = 2.54e−4 mm.

ate at the tip or tips of the pre-existing cracks whose locations are closest to the disc centre. Second, the cracks tend to coalesce from the initiated tip to the midpoint of the pre-existing cracks nearby with this 20 mm spacing. Third, although the artificial material in Fig. 15a already has a high degree of homogeneity, the crack path is not as regular and predictable as in DLSM. In such a discrete particle model, each particle can be ensured to have identical properties. Therefore, it can prevent heterogeneity and is more suitable than the experiment to objectively investigate crack propagation and coalescence regarding the influences from pre-existing cracks in terms of length, spacing, inclination angle, plane roughness, etc.

4.2. Dynamic crack propagation

4.2.1. Crack propagation on PMMA plates

Dynamic crack propagation is illustrated with perforated plates. The simulated material properties are as follows: an elastic modulus of 35 GPa, a Poisson's ratio of 0.21, and a density of 2.45 g/cm^3. A 400 mm-wide and 200 mm-high thin plate model is built with

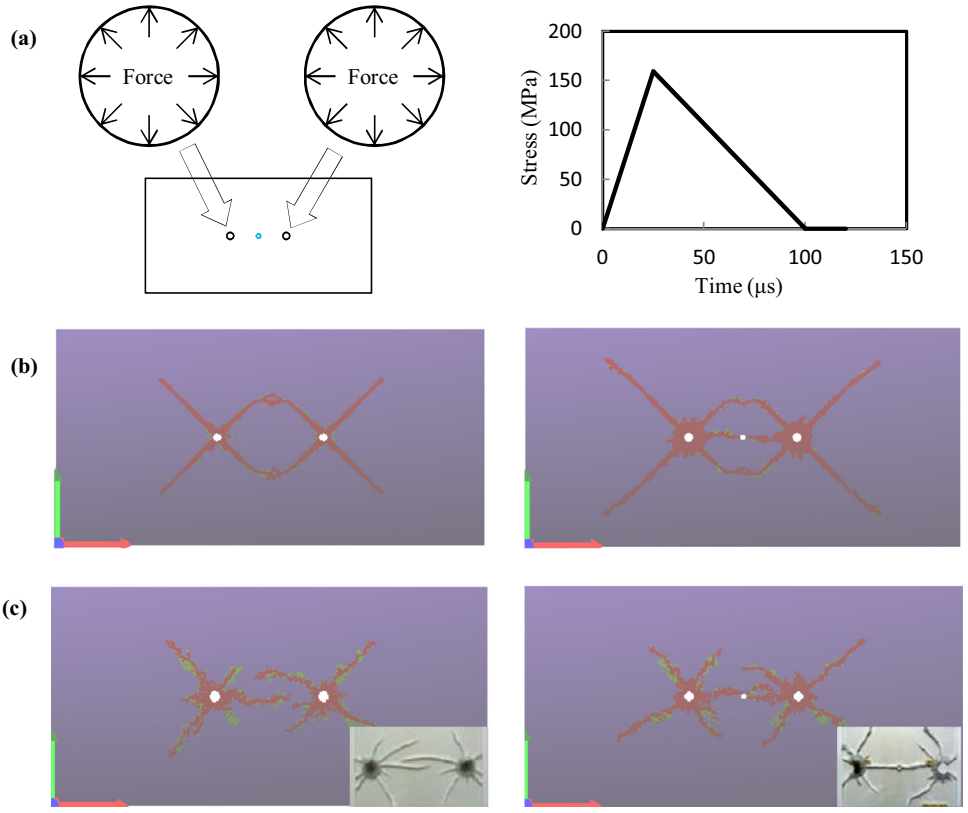

Fig. 16. (a) Boundary condition at the two perforated holes in the plate. (b) Blasting in homogeneous plates (c) Blasting in plates with percentage spatial inhomogeneity of 20% and strength ratio of 3. The results related to PMMA at the corners are from Nakamura et al. (2004); Simulation particle diameter = 1 mm.

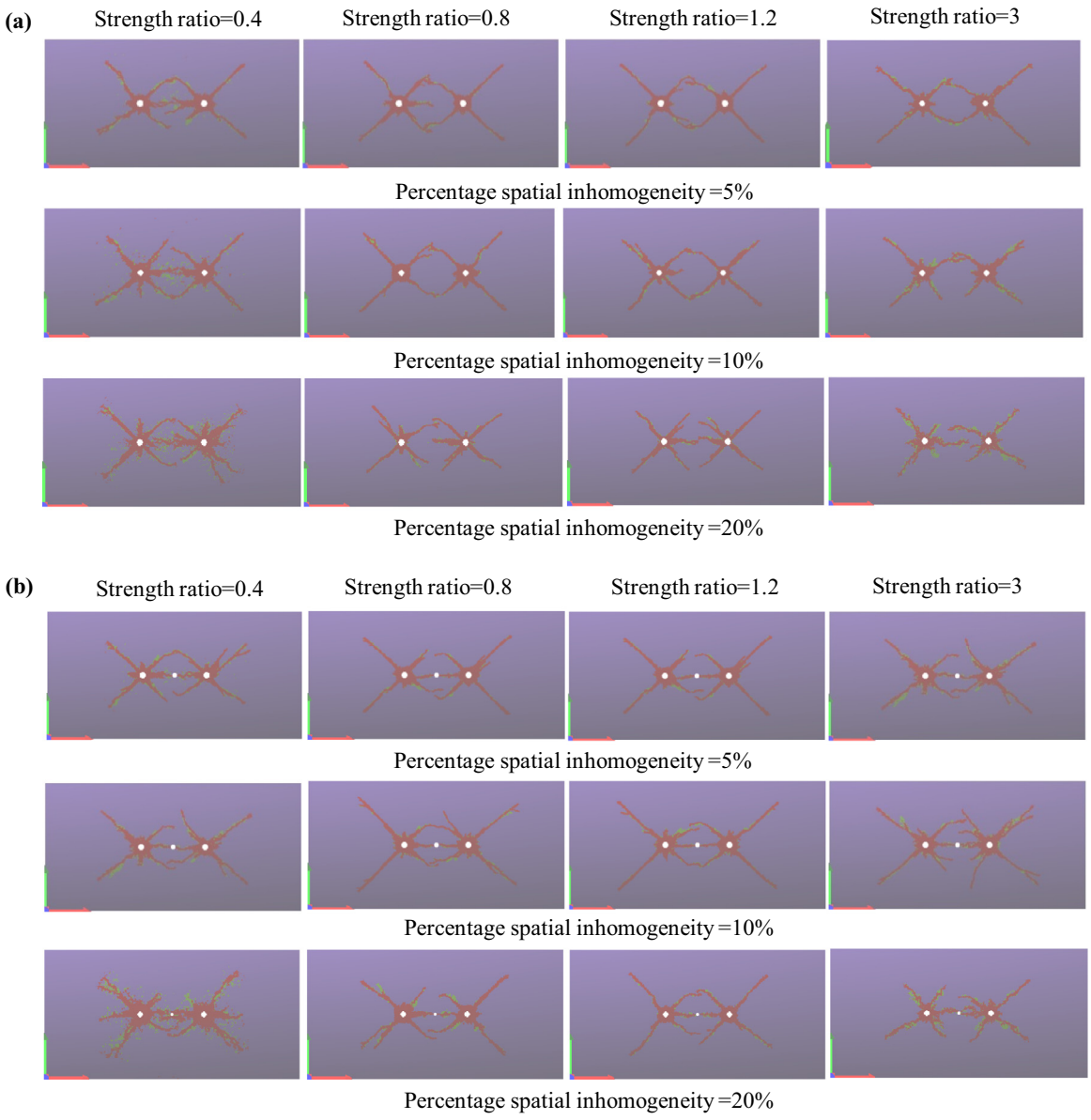

Fig. 17. Crack patterns with different percentage spatial inhomogeneity and strength ratios. (a) Blasting in double holes on a plate (b) Blasting in double holes on a plate with an additional tiny hole in the middle; Simulation particle diameter =1 mm.

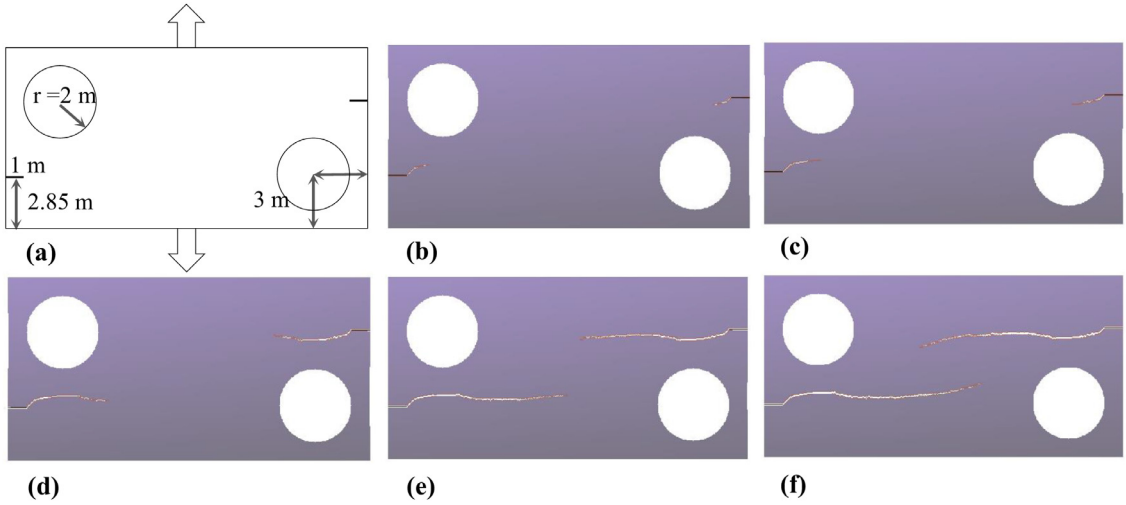

Fig. 18. Geometry and crack propagation of the classic double perforated plate with multiple pre-existing cracks. The original model of 20 m × 10 m has been scaled to 20 mm × 10 mm with particle diameter of 0.03125 mm and $Un^* = 1e{-}5$ mm.

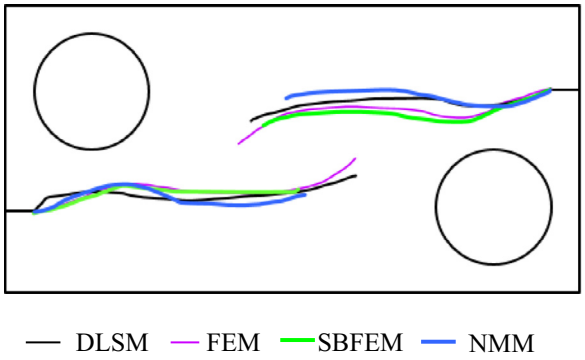

Fig. 19. Comparison of the crack path simulated by different numerical methods – FEM from Miehe et al. (2007), NMM from Zhang et al. (2010), SBFEM from Ooi et al. (2012).

two perforated holes (10 mm in diameter) positioned symmetrically 100 mm apart, and the blasting forces as pulses are applied outwards evenly around the boundaries of two larger holes (see Fig. 16a). In the second example, a third additional hole (6 mm in diameter) is added in the centre. The regular lattice structure generates isotropic material for elastic deformation but causes directional preference on crack propagation due to the anisotropy of the failure surface (see Fig. 16b). This anisotropy problem also exists in other LSMs if it is with regular packing, e.g. the lattice solid model by Mora and Place (1993). The crack patterns on polymethyl methacrylate (PMMA) from Nakamura et al. (2004) are more natural and free of directional dependency (refer to the small pictures in Fig. 16c), which may be attributed to the randomly distributed imperfections in the material. Base on this assumption, a two-phase stochastic generation method is introduced, in which two kinds of material properties are randomly assigned to the model; one represents the base material and the other is the material with other strength. The model is still homogeneous before the cracking because the second material has the same elastic material properties of the base material. The directional preference can be relieved by introducing the randomly distributed second material. Influences of the percentage spatial inhomogeneity and strength ratio are shown in Fig. 17. As shown in Fig. 17, in general when the strength ratio diverges from one, the direction dependence of fracturing is reduced. However, to reproduce the experimental crack patterns very high level of spatial inhomogeneity (20%) and large differences in the strength properties (ratio of 3) are needed, which is a shortcoming of DLSM with regular lattice structure.

4.2.2. Crack propagation on a classic perforated model

The second example involves a classic numerical problem first presented by Bouchard et al. (2000) with two perforated holes and

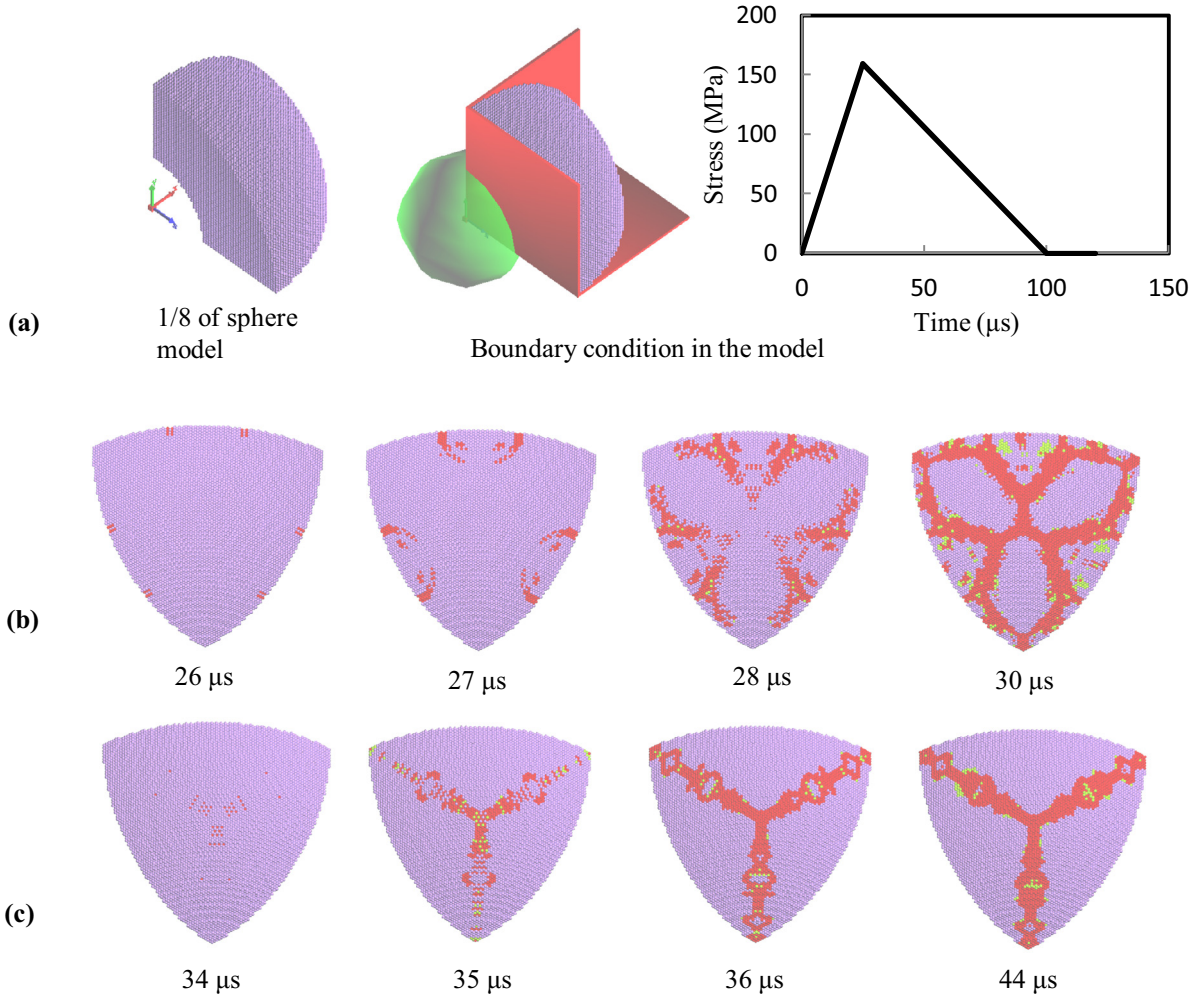

Fig. 20. Simulation results in a 3D volume. (a) 3D Blasting model and its boundary condition. The red is the fixed boundary to the normal direction, and the green is the applied force, where its magnitude with time is shown on the right. (b) Development of the crack on the surface with $Un^* = 2.5e{-}3$ mm(c) Development of the crack on the surface with $Un^* = 3.5e{-}3$ mm; Particle diameter is 1 mm.

two pre-existing cracks on the edges (refer to Fig. 18a). The simulated material has the properties of E = 10 GPa and $\upsilon = 0.3$. The model is subject to tension on the upper and bottom boundaries. It can be observed from Fig. 18b-f that the cracks initiate at the tips of the pre-existing cracks and tilt to the adjacent holes in the early steps. They then propagate almost symmetrically. Fig. 19 draws the crack paths obtained from different numerical methods, i.e., the finite element method (FEM) from Miehe et al. (2007), numerical manifold method (NMM) from Zhang et al. (2010), scaled boundary finite element method (SBFEM) from Ooi et al. (2012) and DLSM. It is noted that different numerical methods generate slightly different crack paths due to different crack propagation criteria or parameters. However, they all provide generally similar and reasonable paths along with DLSM.

4.2.3. Crack propagation on a 3D sphere

The last example is the blasting inside a 3D spherical shell. The scenario is an exploration of a spherical blasting source (40 mm in diameter) filled to the core of a sphere 100 mm in diameter. The material in this example is homogeneous so that the model can be simplified to 1/8 of the actual scenario due to symmetry. The model and its boundary conditions are shown in Fig. 20a. The green sphere indicates the blasting source, of which only 1/8 has an effect on the model. The red boundaries restrict the displacement in the corresponding normal directions. Two different threshold values for a normal spring (Un^*) are adopted in two cases to represent weak or strong material, and the simulated results are recorded in time sequences in Fig. 20b and c, respectively. In comparison, the crack propagation in weak material (Fig. 20b) arrives at the surface of the sphere 8 μs earlier than that in strong material (Fig. 20c). This is because the crack initiates earlier in the weak material because the normal spring is easier to break than the relatively strong material. The total area of the crack also indicates that the cracks are dispersed in the weak material, whereas they are relatively concentrated in the strong material. This could be explained at the particle scale. When the blasting energy approaches with a strain wave, the springs dissipate the energy by its deformation until the maximum spring potential energy is exceeded. Therefore, weak material with smaller Un^* must sacrifice more springs to dissipate the same amount of energy, leading to a dispersed crack pattern.

These three examples show the ability of DLSM in simulating dynamic cracks in both 2D and 3D. The dynamic fracture broadly occurs in many engineering fields such as hydraulic fracturing and tunnel blasting, and the advantage of DLSM is to build a complex geology model to investigate the crack phenomena in a simple manner.

5. Conclusion and remarks

In this paper, DLSM is employed for investigating crack propagation in brittle materials. The relationship between the simple fracturing law in DLSM and the crack criterion in classic fracture mechanics is investigated for the first time. First, through the correlation of the spring deformation in DLSM and stress intensity factor in LEFM, it is proved that the mechanism in DLSM is valid for the fracture problem. Second, as in the literature, the calculated mode I fracture toughness is inconsistent for materials with different geometries in DLSM. The numerical simulations reveal that a large portion of the degree of inconsistency is associated with the intrinsic length-scale of the microstructure of the material. Third, in DLSM, a simple one-parameter fracturing law with a normal spring reproduces the fracture pattern and failure loads of a synthetic rock in mode I, mixed mode, and mode II crack tests that involve both tensile and shear cracks; thus, it is unnecessary to decompose crack criteria into different fracture modes in DLSM, and crack propagation detection becomes easier. DLSM is then further validated through examples with multiple pre-existing cracks to investigate the crack propagation and coalescence, and the results are reasonably matched to the experiment from the literature. Finally, dynamic crack propagation is investigated through perforated plates in 2D and a part of a sphere in 3D, from which the advantages of DLSM are highlighted.

Although DLSM has proved its capability in fracture problems, it is undeniable that some problems exist. The most concerning problem lies in the constitutive model between the particles. Although simulations in this paper with the simple fracturing law work well for brittle materials, when this method is actually applied to elasto-plastic materials, the cohesive model may be more suitable. However, the most appropriate constitutive model must be obtained through experimental validation. The existing testing methods or standards for the fracture problem are mostly designed to serve conventional fracture mechanics (i.e., acquiring macro-parameters for materials), whereby special experiments are desired for the calibration purpose for discontinuum-based models. The authors suggest further work on the micro-constitutive model and related experiments.

Appendix

In this appendix, the calculations of stress intensity factors involved in ANSYS and DLSM are presented.

Firstly, the linear displacement extrapolation method by Eqs. (13) and (14) is used in the regularly meshed ANSYS model to calculate the stress intensity factor in mode I and mode II. The simulated model is a 100 mm-square in plane stress condition subject to 100 MPa tensile stress and 100 MPa shear stress as shown in Fig. 2a. The crack length is 40 mm. In the linear extrapolation, two node sets are required. For simplicity, the ratio of the distance

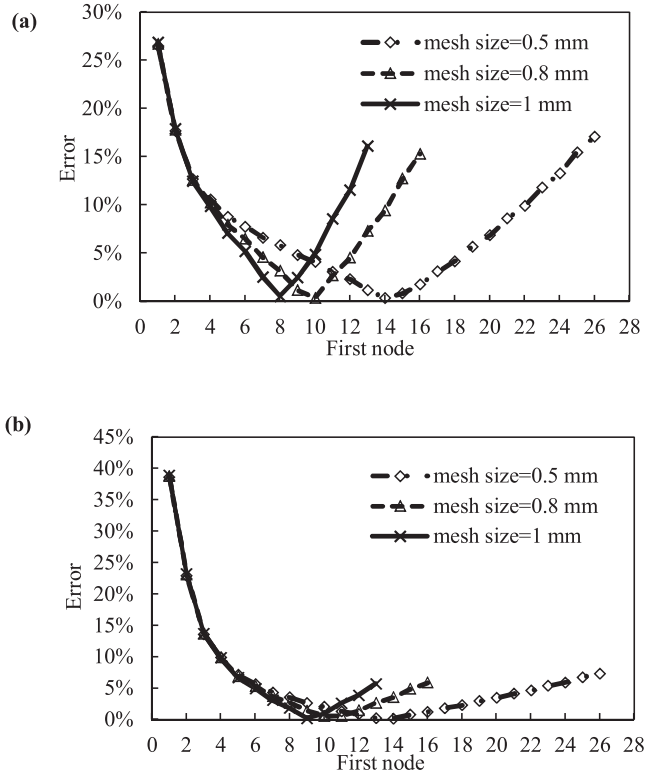

Fig. A1. The errors in calculation of stress intensity factor by displacement extrapolation method at a fixed distance ratio of 1.5. (a) K_I calculation errors (b) K_{II} calculation errors.

Table A1
Errors of stress intensity factors by displacement extrapolation method in models with different crack length and inclination angles. Mesh size is 1 mm.

Crack length(mm)	Inclination = 30°		Inclination = 45°		Inclination = 60°	
	Mode I	Mode II	Mode I	Mode II	Mode I	Mode II
40	2.9%	0.4%	2.2%	0.8%	0.8%	0.2%
60	2.2%	0.6%	0.6%	0.4%	3.9%	3.5%
80	2.7%	0.0%	0.3%	0.3%	1.2%	1.0%

Table A2
The values of K_I calculated by FEM and DLSM and the errors in DLSM as well as the crack opening displacement at the crack tip.

		Particle size = 1 mm			Particle size = 0.5 mm		
Crack length(mm)	K_I(ANSYS) (MPa.m$^{0.5}$)	K_I(DLSM) (MPa.m$^{0.5}$)	Error	$U_{cod\text{-}tip}$ (mm)	K_I(DLSM) (MPa.m$^{0.5}$)	Error	$U_{cod\text{-}tip}$ (mm)
40	0.431	0.430	0.36%	5.32E−05	0.438	1.64%	3.49E−05
50	0.452	0.448	0.89%	5.56E−05	0.457	1.20%	3.64E−05
60	0.462	0.457	1.07%	5.68E−05	0.467	1.02%	3.72E−05
70	0.467	0.462	0.97%	5.74E−05	0.471	1.04%	3.75E−05
80	0.471	0.469	0.42%	5.81E−05	0.477	1.37%	3.79E−05

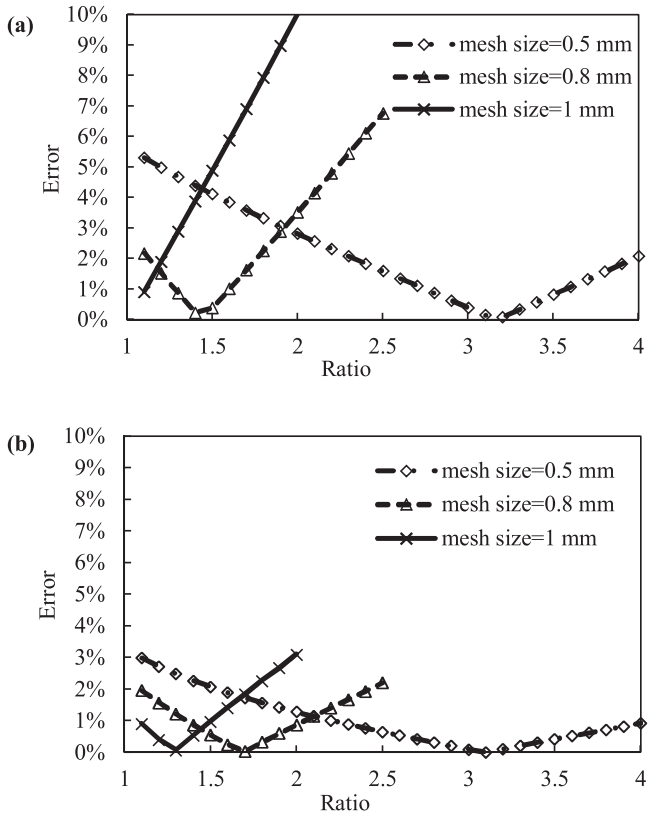

Fig. A2. The errors in calculation of stress intensity factor by displacement extrapolation method fixing the first node at 10th node (a) K_I calculation errors (b) K_{II} calculation errors.

from crack tip to the two nodes is set to an intermediate value of 1.5 (i.e. $L_{crack\ tip\ to\ second\ node}/L_{crack\ tip\ to\ first\ node} = 1.5$). The errors are calculated in three mesh sizes (0.5 mm, 0.8 mm and 1 mm) and plotted in Fig. A1. It is noted that the choice of the 10th node as the first node in linear extrapolation gives a satisfied results among the three resolutions (all the errors < 5%). In addition, when setting the 10th node as the first node in the calculation, different ratios are examined. As noted in Fig. A2, the ratio of 1.5 provides the acceptable error (< 5%). Therefore, the 10th node and the 15th node are the preliminary choice.

Secondly, the choice of nodes is subject to the tests to examine whether it is susceptible to rotation. The mesh size is 1 mm in these examples. The crack with length of 40 mm is rotated 30°, 45° and 60°, respectively. The errors are summed in Table A1 which shows it is still suitable with rotations.

Thirdly, the same strategy is applied to DLSM in calculating SIF in mode I only. The crack length varies from 40 mm to 80 mm, and results for two particle size (0.5 mm and 1 mm) are summarised in Table A2. It is noted that the errors to the FEM solution is low (< 2%).

References

Aliha, M.R.M., Ayatollahi, M.R., 2011. Mixed mode I/II brittle fracture evaluation of marble using SCB specimen. In: 11th International Conference on the Mechanical Behavior of Materials (ICM11), pp. 311–318. doi:10.1016/j.proeng.2011.04.054.

Atkinson, C., Smelser, R.E., Sanchez, J., 1982. Combined mode fracture via the cracked Brazilian disk test. Int. J. Fract. 18, 279–291. doi:10.1007/BF00015688.

Ayatollahi, M.R., Aliha, M.R.M., 2007. Fracture toughness study for a brittle rock subjected to mixed mode I/II loading. Int. J. Rock Mech. Min. Sci. 44, 617–624. doi:10.1016/j.ijrmms.2006.10.001.

Backers, T., 2005. Fracture Toughness Determination and Micromechanics of Rock Under Mode I and Mode II Loading PhD thesis. University of Potsdam.

Bazant, Z.P., Cedolin, L., 1979. Blunt crack band propagation in finite element analysis ASCE. J. Eng. Mech. Div. 105, 297–315.

Beale, P.D., Srolovitz, D.J., 1988. Elastic fracture in random materials. Phys. Rev. B 37, 5500–5507.

Bouchard, P.O., Bay, F., Chastel, Y., Tovena, I., 2000. Crack propagation modelling using an advanced remeshing technique. Comput. Meth. Appl. Mech. Eng. 189, 723–742. doi:10.1016/S0045-7825(99)00324-2.

Chan, S.K., Tuba, I.S., Wilson, W.K., 1970. On the finite element method in linear fracture mechanics. Eng. Fract. Mech. 2, 1–17. doi:10.1016/0013-7944(70)90026-3.

Cotterell, B., Rice, J.R., 1980. Slightly curved or kinked cracks. Int. J. Fract. 16, 155–169. doi:10.1007/BF00012619.

Cundall, P.A., 1971. A computer model for simulating progressive, large-scale movements in blocky rock systems. In: Proceedings of the international symposium on rock fracture, Nancy. International Society for Rock Mechanics (ISRM), pp. 129–136.

Davies, P., Blackman, B.R.K., Brunner, A.J., 1998. Standard test methods for delamination resistance of composite materials: Current status. Appl. Compos. Mater. 5, 345–364. doi:10.1023/A:1008869811626.

Dolbow, J.E., Gosz, M., 2002. On the computation of mixed-mode stress intensity factors in functionally graded materials. Int. J. Solids Struct. 39, 2557–2574. doi:10.1016/S0020-7683(02)00114-2.

Donzé, F., Magnier, S.-A., 1995. Formulation of a 3-D numerical model of brittle behaviour. Geophys. J. Int. 122, 790–802. doi:10.1111/j.1365-246X.1995.tb06838.x.

Fowell, R.J., 1995. Suggested method for determining mode I fracture toughness using Cracked Chevron Notched Brazilian Disc (CCNBD) specimens. Int. J. Rock Mech. Min. Sci. Geomech. Abstr. 32, 57–64. doi:10.1016/0148-9062(94)00015-U.

Fu, P., Johnson, S.M., Settgast, R.R., Carrigan, C.R., 2012. Generalized displacement correlation method for estimating stress intensity factors. Eng. Fract. Mech. 88, 90–107. doi:10.1016/j.engfracmech.2012.04.010.

Griffith, A.A., 1921. The phenomena of rupture and flow in solids philosophical transactions of the royal society of london a: mathematical. Phys. Eng. Sci. 221, 163–198. doi:10.1098/rsta.1921.0006.

Gui, Y., Zhao, G.F., 2015. Modelling of laboratory soil desiccation cracking using DLSM with a two-phase bond model. Comput. Geotech. 69, 578–587. doi:10.1016/j.compgeo.2015.07.001.

Haeri, H., Khaloo, A., Marji, M.F., 2015. Experimental and numerical analysis of Brazilian discs with multiple parallel cracks. Arabian J. Geosci. 8, 5897–5908. doi:10.1007/s12517-014-1598-1.

Haeri, H., Shahriar, K., Marji, M.F., Moarefvand, P., 2014. Experimental and numerical study of crack propagation and coalescence in pre-cracked rock-like disks. Int. J. Rock Mech. Min. Sci. 67, 20–28. doi:10.1016/j.ijrmms.2014.01.008.

Hillerborg, A., Modéer, M., Petersson, P.E., 1976. Analysis of crack formation and crack growth in concrete by means of fracture mechanics and finite elements. Cem. Concr. Res. 6, 773–781. doi:10.1016/0008-8846(76)90007-7.

Hrennikoff, A., 1941. Solution of problems of elasticity by the framework method. J. Appl. Mech. 8, 169–175.

Irwin, G., 1957. Analysis of stresses and strains near the end of a crack traversing a plate. J. Appl. Mech. 24, 361–364.

Jiang, C., Zhao, G.-F., Zhu, J., Zhao, Y.-X., Shen, L., 2016. Investigation of dynamic crack coalescence using a Gypsum-Like 3D printing material rock. Mech. Rock Eng. 49, 3983–3998. doi:10.1007/s00603-016-0967-3.

Lim, I.L., Johnston, I.W., Choi, S.K., Boland, J.N., 1994a. Fracture testing of a soft rock with semi-circular specimens under three-point bending. Part 1—mode I. Int. J. Rock Mech. Min. Sci. Geomech. Abstr. 31, 185–197. doi:10.1016/0148-9062(94)90463-4.

Lim, I.L., Johnston, I.W., Choi, S.K., Boland, J.N., 1994b. Fracture testing of a soft rock with semi-circular specimens under three-point bending. Part 2—mixed-mode. Int. J. Rock Mech. Min. Sci. Geomech. Abstr. 31, 199–212. doi:10.1016/0148-9062(94)90464-2.

Lisjak, A., Grasselli, G., 2014. A review of discrete modeling techniques for fracturing processes in discontinuous rock masses. J. Rock Mech. Geotech. Eng. 6, 301–314. doi:10.1016/j.jrmge.2013.12.007.

Miehe, C., Gurses, E., Birkle, M., 2007. A computational framework of configurational-force-driven brittle fracture based on incremental energy minimization. Int. J. Fract. 145, 245–259. doi:10.1007/s10704-007-9078-1.

Mora, P., Place, D., 1993. A lattice solid model for the nonlinear dynamics of earthquakes. Int. J. Modern Phys. C 04, 1059–1074. doi:10.1142/s0129183193000823.

Nakamura, Y., Cho, S.H., Yoneoka, M., Yamamoto, M., Kaneko, K., 2004. Model experiments on crack propagation between two charge holes in blasting. Sci. Technol. Energetic Mater. 65, 34–39.

Ooi, E.T., Song, C., Tin-Loi, F., Yang, Z., 2012. Polygon scaled boundary finite elements for crack propagation modelling. Int. J. Numer. Methods Eng. 91, 319–342. doi:10.1002/nme.4284.

Parks, D.M., 1974. A stiffness derivative finite element technique for determination of crack tip stress intensity factors. Int. J. Fract. 10, 487–502. doi:10.1007/bf00155252.

Potyondy, D.O., Cundall, P.A., 2004. A bonded-particle model for rock. Int. J. Rock Mech. Min. Sci. 41, 1329–1364. doi:10.1016/j.ijrmms.2004.09.011.

Rao, B.N., Rahman, S., 2003. Mesh-free analysis of cracks in isotropic functionally graded materials. Eng. Fract. Mech. 70, 1–27. doi:10.1016/S0013-7944(02)00038-3.

Rao, Q.H., Sun, Z.Q., Stephansson, O., Li, C.L., Stillborg, B., 2003. Shear fracture (Mode II) of brittle rock. Int. J. Rock Mech. Min. Sci. 40, 355–375. doi:10.1016/S1365-1609(03)00003-0.

Rice, J.R., 1968. A path independent integral and the approximate analysis of strain concentration by notches and cracks. J. Appl. Mech. 35, 379–386.

Shi, G., Goodman, R.E., 1988. Discontinuous deformation analysis - a new method for computing stress, strain and sliding of block systems. Paper presented at the The 29th U.S. Symposium on Rock Mechanics.

Song, S.H., Paulino, G.H., 2006. Dynamic stress intensity factors for homogeneous and smoothly heterogeneous materials using the interaction integral method. Int. J. Solids Struct. 43, 4830–4866. doi:10.1016/j.ijsolstr.2005.06.102.

Srolovitz, D.J., Beale, P.D., 1988. Computer Simulation of Failure in an Elastic Model with Randomly Distributed Defects. J. Am. Ceram. Soc. 71, 362–369. doi:10.1111/j.1151-2916.1988.tb05055.x.

Than, K., 2013. Bangladesh building collapse due to shoddy construction. National Geogr. News. http://news.nationalgeographic.com/news/2013/13/130425-bangladesh-dhaka-building-collapse-world/. Accessed 10 June 2016.

The Welding Institute, 2017. Schenectady T2 tanker. http://www.twi-global.com/news-events/case-studies/schenectady-t2-tanker-165/. Accessed 3 Feb 2017.

Theocaris, P.S., Papadopoulos, G.A., 1984. The influence of geometry of edge-cracked plates on KI and KII components of the stress intensity factor, studied by caustics. J. Phys. D 17, 2339.

Tutluoglu, L., Keles, C., 2011. Mode I fracture toughness determination with straight notched disk bending method. Int. J. Rock Mech. Min. Sci. 48, 1248–1261. doi:10.1016/j.ijrmms.2011.09.019.

Wang, Q.Z., Zhang, S., Xie, H.P., 2010. Rock dynamic fracture toughness tested with holed-cracked flattened brazilian discs diametrically impacted by SHPB and its size effect. Exp. Mech. 50, 877–885. doi:10.1007/s11340-009-9265-2.

Zhang, H.H., Li, L.X., An, X.M., Ma, G.W., 2010. Numerical analysis of 2-D crack propagation problems using the numerical manifold method. Eng. Anal. Boundary Elem. 34, 41–50. doi:10.1016/j.enganabound.2009.07.006.

Zhao, G.-F., 2017. Developing a four-dimensional lattice spring model for mechanical responses of solids. Comput. Meth. Appl. Mech. Eng. 315, 881–895. doi:10.1016/j.cma.2016.11.034.

Zhao, G.F., 2010. Development of Micro-Macro Continuum-Discontinuum Coupled Numerical Method PhD thesis. ÉCOLE POLYTECHNIQUE FÉDÉRALE DE LAUSANNE.

Zhao, G.F., Fang, J., Zhao, J., 2012. A MLS-Based lattice spring model for simulating elasticity of materials. Int. J. Comput. Methods 9. doi:10.1142/S0219876212500375.

Zhao, G., Fang, J., Sun, L., Zhao, J., 2013. Parallelization of the distinct lattice spring model. Int. J. Numer. Anal. Methods Geomech. 37 (1), 51–74.

Zhao, G.F., Fang, J.N., Zhao, J., 2011. A 3D distinct lattice spring model for elasticity and dynamic failure. Int. J. Numer. Anal. Methods Geomech. 35 (8), 859–885. doi:10.1002/nag.930.

Zhao, G.F., Khalili, N., 2012a. Graphics processing unit based parallelization of the distinct lattice spring model. Comput. Geotech. 42, 109–117. doi:10.1016/j.compgeo.2012.01.004.

Zhao, G.F., Khalili, N., 2012b. A Lattice Spring Model for Coupled Fluid Flow and Deformation Problems in Geomechanics. Rock Mech. Rock Eng. 45, 781–799. doi:10.1007/s00603-012-0291-5.